









## On The Nature of Einstein Probe Transient EP250916a: Insights from X-ray, Optical, and Radio Observations

GAURAVA K. JAISAWAL <sup>1</sup>, GIULIA ILLIANO <sup>2</sup>, FRANCESCO CAROTENUTO <sup>3</sup>, ASTRID L. BOUQUIN,<sup>1,4</sup>  
DAVID M. RUSSELL <sup>5</sup>, GIORGOS LELOUDAS <sup>1</sup>, ANDREA SANNA <sup>6</sup>, DALYA AKL <sup>5</sup>, ROB FENDER,<sup>7</sup> AND  
SARA MOTTA <sup>2</sup>

<sup>1</sup>*DTU Space, Technical University of Denmark, Ørstedes Plads 348, DK-2800 Lyngby, Denmark*

<sup>2</sup>*INAF-Osservatorio Astronomico di Brera, Via Bianchi 46, I-23807, Merate (LC), Italy*

<sup>3</sup>*INAF, Osservatorio Astronomico di Roma, Via Frascati 33, I-00078 Monte Porzio Catone, Italy*

<sup>4</sup>*Nordic Optical Telescope, Rambla José Ana Fernández Pérez 7, 38711 Breña Baja, Spain*

<sup>5</sup>*Center for Astrophysics and Space Science (CASS), New York University Abu Dhabi, PO Box 129188, Abu Dhabi, UAE*

<sup>6</sup>*Dipartimento di Fisica, Università degli Studi di Cagliari, SP Monserrato-Sestu km 0.7, I-09042 Monserrato, Italy*

<sup>7</sup>*Astrophysics, Department of Physics, University of Oxford, Keble Road, Oxford, OX1 3RH, UK*

### ABSTRACT

We report multi-wavelength studies of the transient EP250916a, detected by the Einstein Probe on 2025 September 16. Located at low Galactic latitude, the source exhibited a rapid X-ray brightening, reaching an unabsorbed 0.5–10 keV flux of  $(6.4 \pm 0.1) \times 10^{-10}$  erg cm<sup>-2</sup> s<sup>-1</sup>, followed by a plateau and a two-stage decay lasting over 40 days. Swift/XRT monitoring shows a persistently hard spectrum ( $\Gamma \approx 1.6$ –2.2) with only modest softening during decay, while a NuSTAR observation confirms a hard-state continuum extending up to 70 keV. Timing analysis of XMM-Newton data reveals a weak quasi-periodic oscillation (QPO) at  $\sim 13$  Hz. No other coherent pulsations or thermonuclear bursts are detected. Broadband spectral modeling favors a nonthermal power-law continuum with partial-covering absorption, and shows no significant thermal disk component. Optical imaging obtained with NOT/ALFOSC, LCO, and GaiaDR3 identifies two faint sources within the 2 arcsec Swift/XRT positional uncertainty. A MeerKAT observation at 1.28 GHz yielded no radio counterpart, with a  $3\sigma$  upper limit of 60  $\mu$ Jy beam<sup>-1</sup>. The combination of a long-lasting outburst, a hard nonthermal X-ray spectrum, a weak QPO detection, the absence of coherent timing features, and faint potential optical counterparts disfavors a stellar-flare or extragalactic origin and supports an accreting compact-object scenario. Comparisons with similar faint, hard-state transients place EP250916a within a growing population of low-luminosity, hard-state black hole X-ray binary candidates.

*Keywords:* X-ray transient sources; X-ray binary stars; Black holes

### 1. INTRODUCTION

High-energy time-domain astrophysics has advanced significantly with the deployment of wide-field X-ray and  $\gamma$ -ray observatories, including the International Gamma-Ray Astrophysics Laboratory (INTEGRAL; C. Winkler et al. 2003), the Neil Gehrels Swift Observatory (N. Gehrels et al. 2004), the Fermi Gamma-ray Space Telescope (W. B. Atwood et al. 2009), the Monitor of All-sky X-ray Image (MAXI; M. Matsuoka et al. 2009), Einstein Probe (W. Yuan et al. 2022), and the Space-based multi-band astronomical Variable Objects Monitor (SVOM;

J.-L. Atteia et al. 2022). These facilities have transformed our understanding of the dynamic high-energy sky, enabling rapid discovery and coordinated follow-up of transients spanning a wide range of luminosities, timescales, and physical origins (see, e.g., M. Revnivtsev et al. 2004; C. Kouveliotou et al. 2012; A. Merloni et al. 2012).

The observed population of transient X-ray sources encompasses a diverse set of astrophysical phenomena. Explosions of massive stars produce relativistic jets and afterglows identified as  $\gamma$ -ray bursts (C. Kouveliotou et al. 2012; P. D’Avanzo 2015). Magnetically active stars can generate impulsive soft X-ray outbursts through large-scale magnetic reconnection events (e.g., H. Mae-

hara et al. 2012; S. Okamoto et al. 2021). In tidal disruption events, the fallback of stellar debris onto supermassive black holes powers luminous, rapidly evolving X-ray emission (see, e.g., S. Komossa 2015). Accretion onto compact objects, including white dwarfs, neutron stars, and black holes, produces short to longer duration X-ray transients whose properties depend on the accretion geometry, magnetic field strength, and mass-transfer rate (W. H. G. Lewin et al. 1997; C. Done et al. 2007; B. E. Tetarenko et al. 2016).

In binary systems, mass transfer from the companion to the compact object can form an accretion disk that emits strongly in X-rays, giving rise to an X-ray binary (XRB). XRBs rank among the brightest persistent and transient X-ray sources in the Galaxy and serve as crucial laboratories for studying accretion physics, jet formation, and relativistic effects in strong gravitational fields (e.g., W. H. G. Lewin et al. 1997). Their outbursts often exhibit pronounced spectral and timing evolution, reflecting changes in the structure of the inner accretion flow (C. Done et al. 2007; A. Bahramian & N. Degeenaar 2023). Classifying newly discovered X-ray transients, therefore, requires discriminating among multiple possible origins, many of which share overlapping X-ray characteristics. Reliable classification depends on rapid, multiwavelength follow-up, including soft-to-hard X-ray coverage and deep optical and infrared observations. This approach is particularly essential for faint or short-lived transients that might otherwise remain undetected.

The Einstein Probe (EP) mission, equipped with the Wide-field X-ray Telescope (WXT), discovered the X-ray transient EP250916a on 2025 September 16 ( $T_0$ =MJD 60934.148; C. Y. Dai et al. 2025a) at low Galactic latitude ( $l = 355.331^\circ$ ,  $b = -4.634^\circ$ ). WXT monitoring revealed a rapid flux increase from  $\sim 3 \times 10^{-11}$  to  $\sim 2 \times 10^{-10}$  erg cm $^{-2}$  s $^{-1}$  within  $\sim 38$  hours (C. Y. Dai et al. 2025b), with a preliminary photon index of  $\Gamma = 1.6 \pm 0.1$ . Follow-up observations with SVOM/MXT on September 17 confirmed continued brightening, measuring a 0.2–10 keV flux of  $3.5 \times 10^{-10}$  erg cm $^{-2}$  s $^{-1}$  with  $\Gamma \approx 2$  and  $N_H \approx 3 \times 10^{21}$  cm $^{-2}$  (A. Coleiro et al. 2025). Subsequent initial Swift/XRT observations refined the source position and measured an unabsorbed 0.3–10 keV flux of  $(6.2 \pm 0.1) \times 10^{-10}$  erg cm $^{-2}$  s $^{-1}$  with  $\Gamma = 1.67 \pm 0.04$  (G. Illiano et al. 2025). A NuSTAR observation on 2025 September 24, further revealed a stable hard-state spectrum extending up to 70 keV (G. K. Jaisawal et al. 2025a).

To investigate the nature of EP250916a and track its long-term evolution, we initiated a coordinated follow-

up campaign with Swift, NuSTAR, and XMM-Newton, supplemented by optical imaging with the Nordic Optical Telescope (NOT) and Las Campanas Observatory (LCO) network. We also monitored the source with *MeerKAT* radio telescope. This campaign provides precise localization, continuous X-ray monitoring, and multiwavelength diagnostics, all of which are essential for constraining the physical origin of the emission from the source. In this paper, we present a temporal and spectral study of the X-ray outburst from EP250916a. Section 2 describes the data acquisition and reduction procedures for Swift, NuSTAR, XMM-Newton, NOT, LCO, and *MeerKAT* observations, including astrometric and photometric inputs from Gaia within the X-ray error box. Section 3 presents the X-ray temporal analysis, light curves, and hardness evolution. Section 4 details the spectral studies with Swift/XRT, NuSTAR, and XMM-Newton. Section 5 discusses the implications of our results, and Section 6 summarizes our conclusions.

## 2. OBSERVATIONS AND DATA ANALYSIS

### 2.1. *Swift*

Follow-up monitoring of EP250916a with the X-Ray Telescope (XRT) onboard the Neil Gehrels Swift Observatory (N. Gehrels et al. 2004) began shortly after the EP detection. XRT operates in two observing modes: photon counting (PC) for faint sources and windowed timing (WT) for brighter sources, allowing both spectral and timing analyses over the 0.2–10 keV energy range across a wide dynamic range. EP250916a was observed from 2025 September 17, 21:35 to November 1, 06:23 (UTC), providing 44 days of coverage ( $T_0+1.8$  to  $T_0+46.3$  days) with a total XRT exposure of approximately 20.6 ks. Observations were carried out simultaneously in the UV/optical bands with the Ultra-Violet/Optical Telescope (UVOT), resulting in a net UVOT exposure of 20.3 ks. XRT data reduction was performed in *HEASoft* v6.35.2 using *xrtpipeline*. Source and background spectra were extracted from both WT and PC mode events with *XSELECT*, and ancillary response files were generated using *xrtmkarf*. PC data with count rates exceeding 0.6 counts s $^{-1}$  were corrected for pile-up by excluding the central region, with the exclusion radius determined by fitting the outer wings of the point spread function with a King function.

EP250916a was clearly detected in the Swift/XRT observations. Its position was initially determined using standard PSF-fitting of PC mode data (total exposure 7.8 ks; panel a of Figure 1) as R.A. (J2000) =  $268.2386^\circ$  ( $17^{\text{h}} 52^{\text{m}} 57.27^{\text{s}}$ ), Dec. (J2000) =  $-35.3231^\circ$  ( $-35^\circ 19' 23.2''$ ), with a 90% confidence error radius of 3.5 arcsec. By refining the XRT position using UVOT

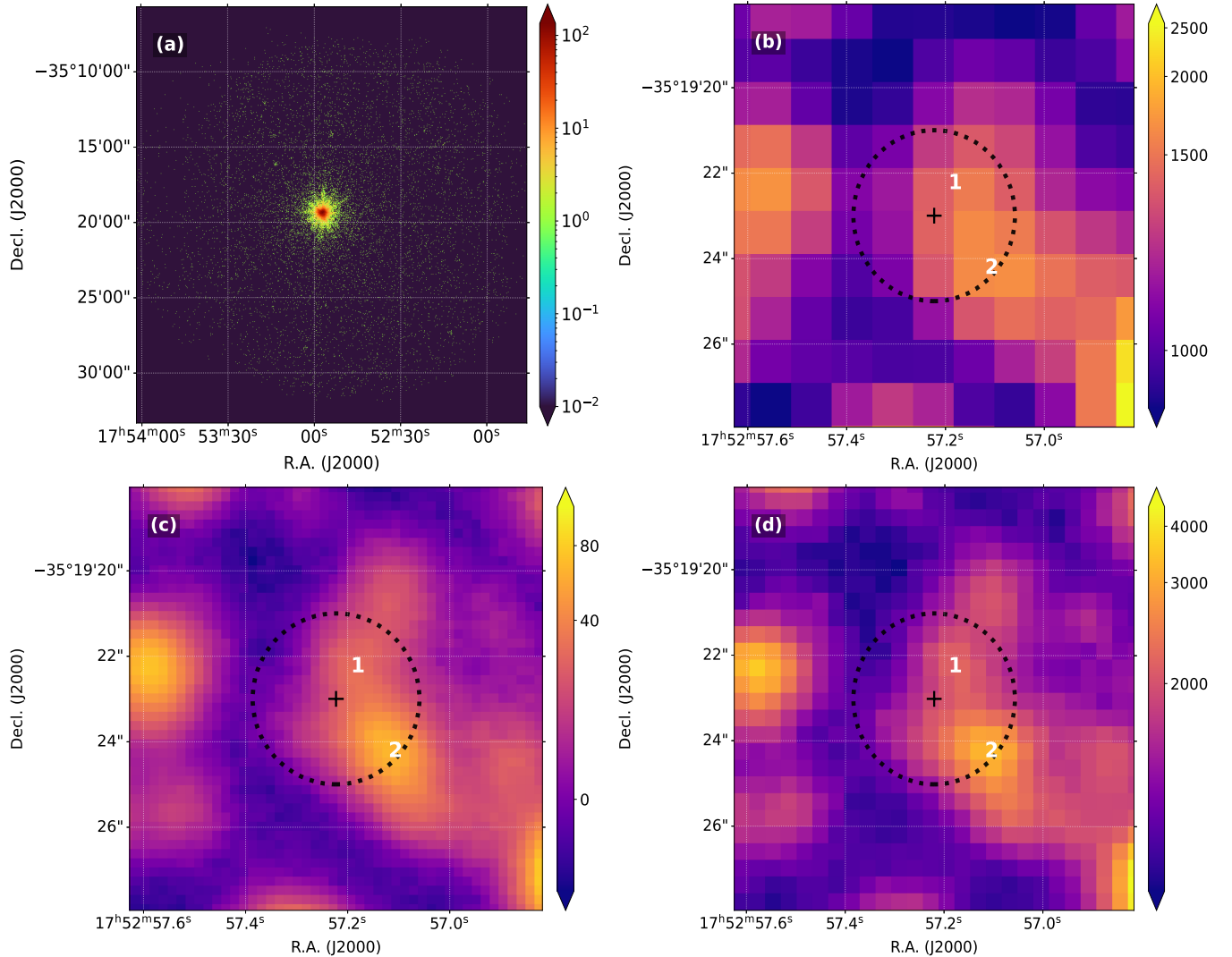


**Figure 1.** The field of EP250916a observed with (a) Swift/XRT (0.5–10 keV). Panels (b), (c), and (d) display zoomed views of the Swift/UVOT (V-band), NOT/ALFOSC R-band, and LCO  $i'$ -filter images, respectively, centered on the Swift/XRT position (marked by a plus sign). Each zoomed-in panel shows a  $\sim 8'' \times 8''$  region centred on the X-ray position. Both Gaia DR3 sources within the 2 arcsec X-ray positional uncertainty (black circle) are also marked.

field astrometry, the coordinates were improved to R.A. (J2000) =  $268.23842^\circ$  ( $17^{\text{h}} 52^{\text{m}} 57.22^{\text{s}}$ ), Dec. (J2000) =  $-35.32306^\circ$  ( $-35^\circ 19' 23.0''$ ), reducing the positional uncertainty to 1.9 arcsec (90% confidence). For details on enhancing X-ray positions with UVOT astrometry, refer to *M. R. Goad et al. (2007)*. The analysis was performed using the online Swift/XRT analysis tools<sup>8</sup> (*P. A. Evans et al. 2009*).

UVOT data were studied following standard procedures<sup>9</sup>. Aspect-corrected images were analyzed using a 2 arcsec source radius and a 5 arcsec background region placed in a source-free area. Multiple exposures were

co-added using the UVOTISUM task to maximize depth. The co-added UVOT images yield AB magnitudes of  $B = 18.7 \pm 0.1$  and  $V = 18.0 \pm 0.1$  mag (see panel b of Figure 1).

## 2.2. NuSTAR

NuSTAR (*F. A. Harrison et al. 2013*) is a grazing-incidence hard X-ray focusing telescope, sensitive in the 3–79 keV energy range. A NuSTAR observation of EP250916a (ObsID 91101336002; PI Jaisawal) was carried out on 2025 September 24 (MJD 60942.476–60942.927;  $T_0+8.6$  days), providing a total exposure of 21 ks. The source was detected at R.A. =  $268.239^\circ$ , Dec. =  $-35.323^\circ$  (J2000), consistent with the localization provided by Swift/XRT. Data reduction was per-

<sup>8</sup> [https://www.swift.ac.uk/user\\_objects/](https://www.swift.ac.uk/user_objects/)

<sup>9</sup> <https://www.swift.ac.uk/analysis/uvot/>

formed using the `HEASoft v6.35.2` package with calibration files version 20251029. Standard processing routines were followed, using `NUPIPELINE` to reprocess the unfiltered event files and `NUPRODUCTS` to extract light curves and spectra from the clean data. We performed barycentric correction using the `barycorr` task and the JPL DE405 ephemerides. Circular source and background regions with a radius of 60 arcsec were used in the analysis. The spectra were grouped to a minimum of 30 photons per channel bin.

### 2.3. XMM-Newton

XMM-Newton (F. Jansen et al. 2001) observed EP250916a on 2025 September 24 (ObsID 0973390201; PI Illiano), covering the time interval 13:44–21:09 UTC (MJD 60942.57–60942.88;  $T_0+8.6$  days), yielding a total exposure of 30.3 ks. During the observation, the EPIC-pn detector (L. Strüder et al. 2001) was operated in fast-timing mode, providing a temporal resolution of 29.5  $\mu$ s. The Observation Data Files were processed using the XMM-Newton Science Analysis Software (SAS v21.0.0). Photon arrival times were corrected to the Solar System barycenter using the `barycen` task and the JPL DE405 ephemerides.

Intervals affected by enhanced soft-proton activity were identified from the 10–12 keV light curves and removed, leaving 26.4 ks of good exposure. Because the EPIC-pn camera provides the highest timing resolution and was unaffected by photon pile-up in fast readout modes, we used only EPIC-pn data for both the timing and spectral analysis. Source events were extracted from a 22-pixel-wide strip (RAWX 26–48), and background from a 10 pixel-wide strip (RAWX 3–13). The spectrum was grouped to a minimum of 100 counts per bin, with a 1% systematic uncertainty added to account for instrumental features, including the Si-K line at 1.84 keV and the Au-M line at 2.2 keV (see the official XMM-Newton User Guide<sup>10</sup>).

### 2.4. Gaia

The Gaia mission, launched by the European Space Agency in 2013, provides precise astrometric, photometric, and spectroscopic measurements for over 1.8 billion sources (Gaia Collaboration et al. 2023). Gaia observes in three primary passbands<sup>11</sup>: the broad G band (330–1050 nm) for astrometry and photometry, and the blue ( $G_{BP}$ ; 330–680 nm) and red ( $G_{RP}$ ; 640–1050 nm) bands for magnitudes and color information.

We cross-matched the refined Swift/XRT position of EP250916a (R.A. = 268.23842°, Dec. = -35.32306°, 90% confidence radius 1.9 arcsec) with the Gaia DR3 catalog. Two Gaia sources lie within 2 arcsec of the XRT position:

- (i) Gaia DR3 4040690560682232064 (Source 1) at coordinates R.A. (J2000) = 268.2382413° and Dec. (J2000) = -35.3228499° is the closest object, located 0.92 arcsec separation from the X-ray transient. It has a high-quality astrometric solution (RUWE<sup>12</sup> of 0.942) and a parallax  $\varpi$  of  $0.7945 \pm 0.2143$  mas, corresponding to a geometric distance of  $D \approx 1.26$  kpc. Its photometry (G = 18.59 mag) indicates a faint Galactic star, with  $G_{BP}-G_{RP}$  color index of  $1.3 \pm 0.1$ .
- (ii) Gaia DR3 4040690560682333568 (Source 2) at coordinates R.A. (J2000) = 268.2379343° and Dec. (J2000) = -35.3234010° lies 1.88 arcsec from the X-ray transient. It has a noisier astrometric solution (RUWE  $\approx 2.7$ ), likely due to unresolved binarity or source multiplicity (K. El-Badry 2025), with a parallax  $\varpi$  of  $-0.905 \pm 0.323$  mas. The object has a photometry magnitude of G = 17.72 mag, with  $G_{BP}-G_{RP}$  color index of  $1.37 \pm 0.03$ .

We also note that four additional faint Gaia sources with G=18.8–19.9 mag are located at angular separations of 2.3–3.5 arcsec, within the standard XRT positional uncertainty. However, given the refined XRT localization of 1.9 arcsec, these objects are less likely to be associated with the X-ray transient. The two Gaia sources, Source 1 and Source 2, are relatively faint, and either could plausibly be the optical counterpart to EP250916a.

### 2.5. Nordic Optical Telescope

The Nordic Optical Telescope (NOT) is a 2.56 m telescope located at the Roque de los Muchachos Observatory on La Palma, Spain. Imaging was obtained with the ALFOSC (Andalucia Faint Object Spectrograph and Camera) instrument, which provides a  $6.4 \times 6.4$  arcmin<sup>2</sup> field of view and a pixel scale of 0.189 arcsec pixel<sup>-1</sup>. A single R-band observation of the EP250916a field was taken on 2025 October 7 at 19:58 UT (MJD 60955.83;  $T_0+21.7$  days) with an exposure time of 600 s. The observation was carried out with a seeing between 1.0–1.5 arcsec with an airmass of 2.91. The data were re-

<sup>10</sup> <https://www.cosmos.esa.int/web/xmm-newton/documentation>

<sup>11</sup> <https://www.cosmos.esa.int/web/gaia/edr3-passbands>

<sup>12</sup> A goodness-of-fit metric that indicates how well a star’s astrometric data matches the single-star model, see K. El-Badry (2025) and references therein.

duced using the PyNOT<sup>13</sup> software, including standard bias subtraction and flat-field correction. Astrometric calibration of the reduced image was performed via the online portal<sup>14</sup> (D. Lang et al. 2010), which matches detected sources to reference catalogs. We calibrated the R-band photometry by cross-matching our detected sources with Gaia DR3 stars ( $10 < G < 16$ ) within a 0.1 deg search radius around the X-ray position of the object. The Gaia G magnitudes were converted to an R-band equivalent using a standard quadratic color term in blue and red filters ( $G_{BP} - G_{RP}$ ). The photometric zero point was derived as the median difference between the transformed Gaia magnitudes and our instrumental magnitudes for the matched stars.

The R-band image is shown in panel (c) of Figure 1. Within the 2 arcsec XRT error circle, we identify a faint optical star with  $R = 17.4 \pm 0.1$  mag (Vega), corresponding to  $R_{AB} \approx 17.6$  mag. This source is consistent with Gaia DR3 4040690560682333568 (Source 2; see section 2.4). A weak emission can also be seen at the position of the first Gaia object (Source 1; Gaia DR3 4040690560682232064), with a  $3\sigma$  limiting magnitude of 18.8 (Vega) in the NOT image (panel c of Figure 1). The reported magnitudes are not corrected for Galactic extinction.

### 2.6. Las Cumbres Observatory

We observed the field of EP250916a with the 1-m Las Cumbres Observatory (LCO) node at Cerro Tololo Inter-American Observatory, Chile, on 2025 September 19 (MJD 60937.03;  $T_0 + 2.9$  days). 200-s exposures were taken in SDSS  $g'$  and  $i'$  filters. The airmass during observation was 1.12, and the seeing was 1.51 arcsec. Data reduction was automatically performed by the **banzai** pipeline. As with the NOT data, astrometric calibration of the reduced image was performed via the online portal. The  $i'$ -band image is shown in panel (d) of Figure 1. Both the Gaia sources (see section 2.4) within the 2 arcsec XRT error region were seen. Photometric calibration of the  $i'$ -band image was performed following the method described in Section 2.5. We detect Source 2 with  $i' = 17.9 \pm 0.1$  mag (Vega). A faint emission is also visible at the position of Source 1, with a  $3\sigma$  limiting magnitude of 19.7 (Vega) in the LCO image (panel d of Figure 1).

### 2.7. MeerKAT

We observed EP250916a with the *MeerKAT* radio telescope (F. Camilo et al. 2018; J. Jonas & MeerKAT

Team 2016) as part of the X-KAT programme (SCI-20230907-RF-01; PIs Fender & Motta), beginning on 2025 September 27 13:24 UT (MJD 60945.558;  $T_0 + 11.4$  days) for a total on-source time of 15 minutes at L-band, with a central frequency of 1.28 GHz and a 875 MHz bandwidth. We used PKS J1939-6342 as the bandpass and flux density calibrator, and PKS 1827-360 as the complex gain calibrator. We reduced the data with the 0xKAT pipeline (I. Heywood 2020), which performs standard flagging, calibration and imaging using **tricolour** (B. V. Hugo et al. 2022), **CASA** (CASA Team et al. 2022) and **WSCLEAN** (A. R. Offringa et al. 2014), respectively. For the imaging part, we adopted a Briggs weighting scheme with a  $-0.3$  robust parameter, yielding a beam of  $7.2'' \times 5.9''$  and a  $20 \mu\text{Jy beam}^{-1}$  rms noise at 1.28 GHz. We do not detect radio emission at the known location of EP250916a, and we place a  $3\sigma$  upper limit on the peak flux density of the target at  $60 \mu\text{Jy beam}^{-1}$ .

## 3. X-RAY TEMPORAL ANALYSIS

### 3.1. X-ray Light curves and hardness-intensity diagram with Swift/XRT

To investigate the long-term temporal evolution of X-ray emission from EP250916a, we extracted Swift/XRT light curves in the soft (0.5–1.5 keV), hard (1.5–10 keV), and full (0.5–10 keV) energy bands. The light curves (top panel of Figure 2, left side) show that the source was already bright at the start of Swift monitoring and reached its observed maximum near MJD 60938. This was followed by a gradual decline, indicating that Swift captured the peak, plateau, and decay phases. The outburst lasted more than 45 days, indicating a long-lived event rather than a short flare.

The hardness ratio (HR), defined as the ratio of hard-to-soft-band count rates, provides a first look at the spectral evolution (bottom panel of Figure 2, left side). During the earliest Swift observations, the HR remained nearly constant despite moderate flux changes, consistent with a stable hard spectral state. After the peak, the HR gradually decreased, indicating mild spectral softening as the source flux declined. A secondary rise and decline in HR around MJD 60956 suggests a subtle late-time change in spectral shape, though the source remained firmly within the hard regime throughout the Swift coverage.

To further quantify the observed spectral evolution, we constructed a hardness–intensity diagram (HID; right side of Figure 2) that plots the hardness ratio against the source intensity in the 0.5–10 keV range. Because Swift did not observe the initial rising phase, the HID traces only the plateau and decay phases. During this interval, EP250916a occupies a relatively confined

<sup>13</sup> <https://github.com/jkrogager/PyNOT>

<sup>14</sup> <https://nova.astrometry.net/>

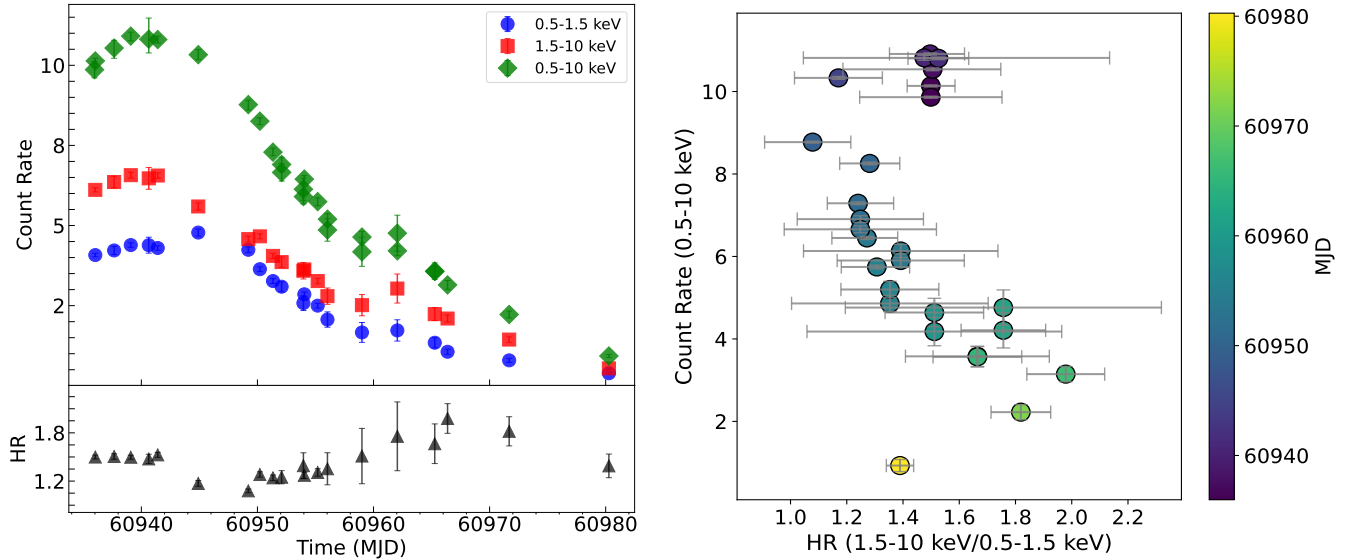


**Figure 2.** Left: Swift/XRT light curves of EP250916a in the 0.5–1.5 keV (soft; blue circles), 1.5–10 keV (hard; red squares), and 0.5–10 keV (full; green diamonds) bands (top), with the corresponding hardness ratio ( $HR = 1.5\text{--}10\text{ keV}/0.5\text{--}1.5\text{ keV}$ ) shown below. Each point represents a single Swift/XRT observation. Right: Hardness–intensity diagram illustrating the spectral evolution of EP250916a during the outburst, color-coded by time (MJD).

region of parameter space, with  $HR \approx 1.2\text{--}2$ , exhibiting only modest changes despite a factor of  $\sim 5$  decrease in intensity. The HID track is smooth, showing slight softening at the highest intensities, followed by a gradual hardening (within error bars) during the decay. The absence of the rising branch in the HID prevents testing for spectral hysteresis, the characteristic “Q-diagram” behavior usually seen in black hole X-ray binaries that undergo full hard-to-soft transitions (J. Homan & T. Belloni 2005). In a typical Q-diagram, the rising branch corresponds to the initial increase in luminosity in the hard state before a transition to the soft state. In the observed interval, EP250916a traces only a single hard-branch track. The rapid rise phase that would form the lower-right leg of the Q-diagram may have occurred before Swift monitoring began. The smooth, monotonic HID evolution is consistent with the modest spectral changes seen in our spectral analysis.

### 3.2. Detection of a quasi-periodic oscillation with XMM-Newton

We extracted the 0.5–10 keV light curve from the XMM-Newton/EPIC-pn data of EP250916a from 2025 September 24, which shows an average count rate of  $98 \pm 4\text{ cts s}^{-1}$ . No type-I X-ray bursts or flares were detected during the observation. We then constructed the power density spectra (PDS). The PDS was normalized such that the integral of each spectrum yields the squared fractional rms variability (power in units of  $\text{rms}^2\text{ Hz}^{-1}$ ). After subtracting the white-noise contribution, the PDS was modeled with multiple Lorentzian

components to characterize the broadband noise (see, e.g., T. Belloni et al. 2002) and to search for potential pulsations or QPO-like features.

The three Lorentzian components were required to fit the data and exhibit the following best-fit parameters with 90% uncertainties. The first, broad component has a centroid frequency of  $\nu_0 = 1.4 \pm 0.1\text{ Hz}$ , a full width at half maximum of  $\Delta = 4.1 \pm 0.5\text{ Hz}$ , and a normalization of  $\text{Norm} = (6.0 \pm 0.2) \times 10^{-3}\text{ rms}^2\text{ Hz}^{-1}$ . The second, broader component is centered at  $\nu_0 = 12 \pm 10\text{ Hz}$ , with a width of  $\Delta = 24 \pm 11\text{ Hz}$  and a normalization of  $\text{Norm} = (5 \pm 1) \times 10^{-4}\text{ rms}^2\text{ Hz}^{-1}$ . These two components describe the source’s underlying broadband variability. The third, narrow Lorentzian is centered at  $\nu_0 = 12.3 \pm 0.7\text{ Hz}$ , with a width of  $\Delta = 4 \pm 3\text{ Hz}$  and a normalization of  $\text{Norm} = (6.6 \pm 0.9) \times 10^{-4}\text{ rms}^2\text{ Hz}^{-1}$ . We tentatively identified this feature as a weak QPO. We then derived a fractional rms of  $7 \pm 3\%$ , a characteristic frequency  $\nu_{\text{max}} = \sqrt{\nu_0^2 + \Delta^2} \approx 12.9 \pm 0.8\text{ Hz}$ , and a quality factor  $Q = \nu_0/(2\Delta) \approx 1.6 \pm 1.2$ , indicating moderate coherence (see, e.g., T. Belloni et al. 2002; A. R. Ingram & S. E. Motta 2019). The PDS (black) and the best-fit model (grey line) are presented in Figure 3. The contributions of the first and second broad Lorentzian components are shown in red and green, respectively, while the third, narrow Lorentzian (blue) accounts for the QPO feature at  $\sim 12.3\text{ Hz}$ . Given its quality factor, we conservatively interpret this feature as either a Type-C-like QPO (see, e.g., A. R. Ingram & S. E. Motta 2019), inner-disk oscillations, or weakly peaked

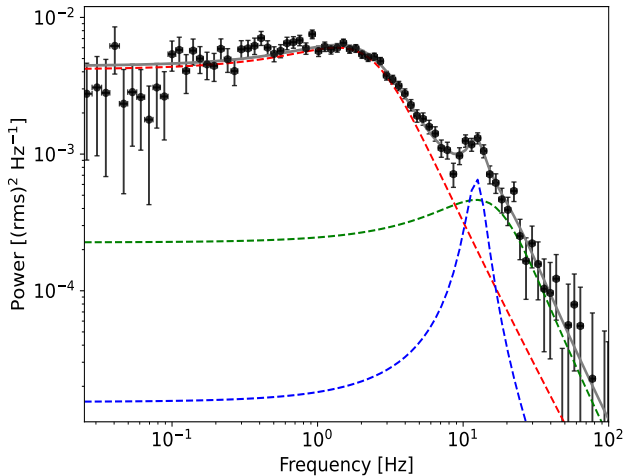


**Figure 3.** PDS (black) of EP250916a using XMM-Newton. The grey line shows the best-fit model with three Lorentzian components. Broad Lorentzians (red and green) describe the underlying noise, while the narrow Lorentzian (blue) indicates a weak QPO at  $\approx 13$  Hz.

noise arising from the corona of an accreting compact object.

### 3.3. NuSTAR timing study

For the NuSTAR observation on 2025 September 24, we extracted light curves in the 3–7, 7–25, 25–50, and 3–70 keV energy bands. The full 3–70 keV light curve exhibits an average count rate of  $\sim 12$  counts  $s^{-1}$ , remaining remarkably stable throughout the exposure. No short-term flares, dips, or thermonuclear bursts were detected in either energy band. To search for coherent or quasi-periodic variability, we computed PDS from barycenter-corrected light curves using Leahy normalization, covering the frequency range  $10^{-3}$ –500 Hz. The PDS is dominated by white (Poisson) noise with an approximately flat slope. Confidence thresholds at  $3\sigma$  and  $5\sigma$  show no significant peaks, ruling out both narrow pulsations and broad QPOs during the observation. These results are consistent across both focal-plane modules and the soft, hard, and full-energy bands.

Motivated by the tentative  $\sim 13$  Hz QPO detected in the XMM-Newton observation (Section 3.2), we performed a sensitivity study to constrain the upper limit on the fractional rms of a QPO at the same frequency in the NuSTAR FPMA and FPMB 3–70 keV light curves. To account for NuSTAR’s instrumental response, we performed Monte Carlo simulations incorporating the detectors’ non-paralyzable dead time. The 1 ms-binned light curves were divided into 1028 s segments, and Leahy-normalized power spectra were computed for each. Using 5000 noise-only simulations, we

established the 95% single-trial detection threshold under dead-time-modified Poisson statistics. Lorentzian QPOs with FWHM of 4 Hz (matching the XMM-Newton measurement) were then injected, and 2500 simulations were performed for each trial fractional-rms amplitude across a finely sampled grid. From the simulations, we derive a 95% confidence upper limit of 3.9% fractional rms for a QPO at  $\sim 13$  Hz in the NuSTAR data. Although this upper limit is lower than the fractional rms amplitude measured with XMM-Newton, it is marginally consistent with the detection considering the uncertainties.

## 4. SPECTRAL ANALYSIS

### 4.1. Outburst Evolution with Swift/XRT

We analyzed the Swift/XRT spectra of EP250916a in the 0.5–10 keV band using XSPEC (K. A. Arnaud 1996). Due to low photon counts in several observations, we employed the Cash statistic (C-stat; W. Cash 1979) for fitting. The spectra were modeled with an absorbed power-law (`tbabs*powerlaw`) using `wilm` abundances (J. Wilms et al. 2000) and `vern` cross sections (D. A. Verner et al. 1996). All parameters, including hydrogen column density  $N_H$ , photon index  $\Gamma$ , and power-law normalization, were allowed to vary. The absorbed power-law model provided statistically acceptable fits across all epochs. We also tested single-component thermal models such as `blackbody` and `diskbb`, which yielded poorer fits, confirming that the X-ray emission is not thermally dominated. These results indicate that the soft X-ray continuum is primarily nonthermal.

The best-fit parameters for each observation are summarized in Table 1, and their temporal evolution is shown in Figure 4. The absorbing column density varies between  $(0.25\text{--}1) \times 10^{22}$   $\text{cm}^{-2}$ , exceeding the Galactic line-of-sight value of  $2.2 \times 10^{21}$   $\text{cm}^{-2}$  (HI4PI Collaboration; HI4PI Collaboration et al. 2016). This excess may indicate intrinsic absorption local to the source, possibly associated with a dense local environment or stellar outflow material. The photon index gradually softens over time, evolving from  $\Gamma \approx 1.6$  before the peak of the outburst to  $\Gamma \approx 2.2$  during the late decay, suggesting a modest spectral softening. We also note that the hardness ratio (Figure 2) shows a slight increase, within uncertainties, during the outburst decay phase. This behavior may be caused by variations in absorption column density (Figure 4), which can attenuate soft X-ray photons. As a result, the hardness ratio may show a modest increase even when the intrinsic spectrum becomes softer, as indicated by the evolution of the photon index.

**Table 1.** Best-fit spectral parameters for Swift/XRT observations using an absorbed power-law model. Errors are quoted at the 90% confidence level. The 0.5-10 keV unabsorbed flux is in the unit of  $\text{erg cm}^{-2} \text{s}^{-1}$ .

ObsIDs	$N_{\text{H}}$ ( $10^{22} \text{ cm}^{-2}$ )	$\Gamma$	$\Gamma_{\text{Norm}}$ ( $10^{-2}$ )	Flux ( $10^{-10}$ )	Cstat (dof)
3000100001	$0.50 \pm 0.10$	$1.59 \pm 0.13$	$8.9 \pm 1.4$	$6.3 \pm 0.3$	94 (67)
3000100002	$0.39 \pm 0.03$	$1.67 \pm 0.04$	$8.7 \pm 0.4$	$5.7 \pm 0.1$	519 (403)
3000100003	$0.41 \pm 0.04$	$1.68 \pm 0.05$	$9.9 \pm 0.6$	$6.4 \pm 0.1$	305 (285)
3000100004	$0.38 \pm 0.03$	$1.68 \pm 0.04$	$9.4 \pm 0.4$	$6.0 \pm 0.1$	451 (384)
3000100005	$0.39 \pm 0.07$	$1.70 \pm 0.09$	$9.5 \pm 1.0$	$6.0 \pm 0.2$	128 (126)
3000100006	$0.37 \pm 0.03$	$1.66 \pm 0.05$	$9.1 \pm 0.5$	$6.0 \pm 0.1$	411 (315)
3000100007	$0.30 \pm 0.04$	$1.79 \pm 0.07$	$9.1 \pm 0.7$	$5.2 \pm 0.1$	222 (183)
3000100008	$0.29 \pm 0.04$	$1.81 \pm 0.07$	$7.6 \pm 0.6$	$4.3 \pm 0.1$	195 (188)
3000100009	$0.33 \pm 0.04$	$1.77 \pm 0.06$	$7.2 \pm 0.5$	$4.3 \pm 0.1$	243 (232)
3000100010	$0.20 \pm 0.10$	$1.63 \pm 0.16$	$5.2 \pm 0.9$	$3.5 \pm 0.2$	50 (50)
3000100011	$0.34 \pm 0.04$	$1.79 \pm 0.07$	$6.2 \pm 0.5$	$3.6 \pm 0.1$	194 (213)
3000100012	$0.25 \pm 0.20$	$1.51 \pm 0.32$	$4.5 \pm 1.6$	$3.5 \pm 0.5$	9 (14)
3000100013	$0.43 \pm 0.05$	$1.94 \pm 0.07$	$6.8 \pm 0.6$	$3.5 \pm 0.1$	234 (193)
3000100014	$0.39 \pm 0.06$	$1.78 \pm 0.09$	$5.3 \pm 0.5$	$3.1 \pm 0.1$	143 (140)
3000100015	$0.27 \pm 0.12$	$1.38 \pm 0.17$	$3.5 \pm 0.7$	$3.2 \pm 0.2$	43 (39)
3000100016	$0.50 \pm 0.15$	$1.88 \pm 0.21$	$5.3 \pm 1.3$	$2.8 \pm 0.2$	22 (31)
3000100017	$0.54 \pm 0.15$	$1.76 \pm 0.20$	$4.5 \pm 1.1$	$2.7 \pm 0.2$	35 (35)
3000100018	$1.06 \pm 0.27$	$2.20 \pm 0.28$	$6.2 \pm 2.1$	$2.6 \pm 0.2$	36 (23)
3000100019	$0.87 \pm 0.27$	$1.93 \pm 0.28$	$5.1 \pm 1.8$	$2.6 \pm 0.2$	27 (22)
3000100021	$0.78 \pm 0.28$	$2.03 \pm 0.30$	$3.3 \pm 1.2$	$1.5 \pm 0.1$	13 (19)
3000100022	$0.58 \pm 0.25$	$2.03 \pm 0.32$	$1.2 \pm 0.5$	$0.56 \pm 0.05$	20 (15)

Furthermore, following a rapid initial brightening to a plateau, the 0.5–10 keV unabsorbed flux exhibits a two-stage evolution during the outburst decay. This behavior suggests evolving conditions in the emission region and possible changes in the emission geometry as the outburst progresses. Incorporating rise-phase measurements from EP/WXT (C. Y. Dai et al. 2025a) and SVOM/MXT (A. Coleiro et al. 2025), and extrapolating them to a common 0.5–10 keV range, we modeled the Swift/XRT flux evolution together with flux from XMM-Newton/EPIC-pn<sup>15</sup>, using a quadruple broken power-law function. This model approximately captures the fast initial rise, plateau, and subsequent decay. The flux is parameterized as

$$F(t) = \begin{cases} A \left(\frac{t}{t_{b1}}\right)^{+\alpha_r} + C, & t \leq t_{b1} \\ A \left(\frac{t}{t_{b1}}\right)^{-\alpha_p} + C, & t_{b1} < t \leq t_{b2} \\ A \left(\frac{t_{b2}}{t_{b1}}\right)^{-\alpha_p} \left(\frac{t}{t_{b2}}\right)^{-\alpha_1} + C, & t_{b2} < t \leq t_{b3} \\ A \left(\frac{t_{b2}}{t_{b1}}\right)^{-\alpha_p} \left(\frac{t_{b3}}{t_{b2}}\right)^{-\alpha_1} \left(\frac{t}{t_{b3}}\right)^{-\alpha_2} + C, & t > t_{b3}, \end{cases}$$

<sup>15</sup> The 0.5–10 keV EPIC-pn spectrum, fitted with an absorbed power-law including a partial covering component and an emission line at 0.71 keV (see Section 4.2).

where  $A$  is the normalization near the first break,  $\alpha_r$  the rise index,  $\alpha_p$  the plateau index,  $\alpha_1$  and  $\alpha_2$  the decay indices,  $t_{b1}$ ,  $t_{b2}$ , and  $t_{b3}$  the break times, and  $C$  a constant baseline flux.

The quadruple broken-power-law model approximately reproduces the overall morphology of the outburst (Figure 5). The initial rise is steep, characterized by  $\alpha_r = 0.9 \pm 0.5$  up to  $t_{b1} = 2.4 \pm 0.5$  d (MJD 60936.5) since its discovery by EP/WXT, consistent with the early rapid increase in emission. This is followed by a shallow plateau with  $\alpha_p = 0.16 \pm 0.05$  lasting until  $t_{b2} = 10.2 \pm 0.5$  d (MJD 60944.4), indicative of a quasi-stable emission phase. The subsequent decay proceeds with index  $\alpha_1 = 0.82 \pm 0.06$  until  $t_{b3} = 35.6 \pm 0.9$  d (MJD 60969.7), after which the flux drops rapidly with a steep index of  $\alpha_2 = 10 \pm 4$ , pointing to an abrupt decline in the dominant emission. The normalization and constant baseline flux are  $A = (6.5 \pm 0.4) \times 10^{-10} \text{ erg s}^{-1} \text{ cm}^{-2}$  and  $C = (4.5 \pm 0.2) \times 10^{-11} \text{ erg s}^{-1} \text{ cm}^{-2}$ , respectively. The fit yields  $\chi^2 = 26$  for 15 degrees of freedom ( $\chi^2_\nu = 1.73$ ). The combination of progressive spectral softening and two-stage flux decay in EP250916a is consistent with the evolution of a transient system moving from an active high-flux state toward a low-flux or quiescent phase.

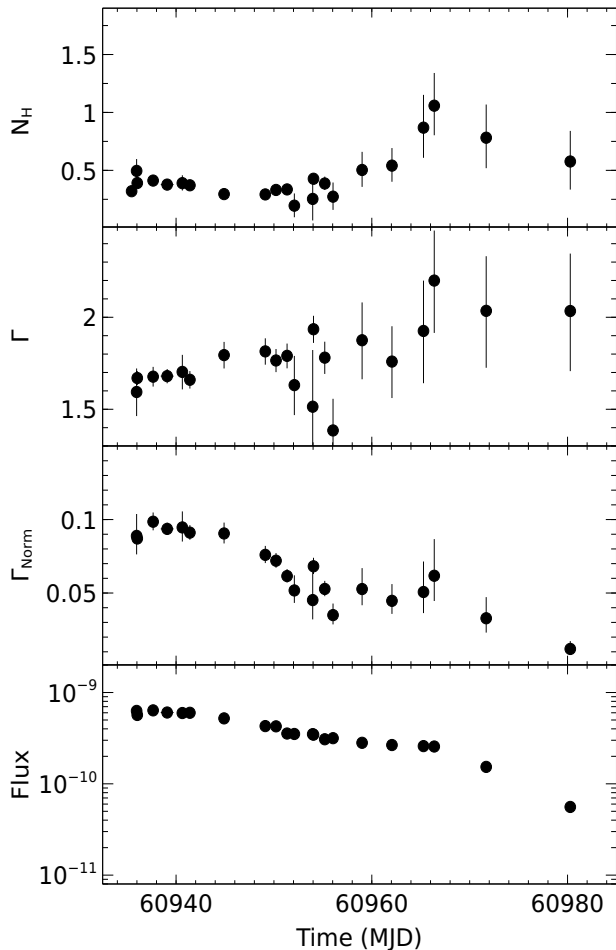


**Figure 4.** Spectral evolution of EP250916a during the outburst from Swift/XRT observations, fitted with an absorbed power-law model. Top to bottom panels show the absorption column density  $N_{\text{H}}$  ( $10^{22} \text{ cm}^{-2}$ ), photon index  $\Gamma$ , normalization ( $\Gamma_{\text{Norm}}$ ), and the 0.5–10 keV unabsorbed flux ( $\text{erg s}^{-1} \text{ cm}^{-2}$ ), respectively.

Such a phenomenological approach has been used to model the outburst light curve of another X-ray transient, EP J182730.0–095633 (H. Q. Cheng et al. 2025), which also exhibited a fast rise followed by a two-stage decay. This modeling can be useful for understanding the temporal evolution of transient outbursts and for comparing the observed decay behavior with disk-instability–driven scenarios (e.g., A. R. King & H. Ritter 1998; G. Dubus et al. 2001).

#### 4.2. Broadband X-ray Spectral Study with *NuSTAR* and *XMM-Newton*

The 3–79 keV *NuSTAR* spectrum of EP250916a can be described by a simple absorbed power-law with hydrogen column density  $N_{\text{H}} = (3 \pm 2) \times 10^{21} \text{ cm}^{-2}$ , photon index  $\Gamma = 2.03 \pm 0.01$  and reduced chi-squared  $\chi^2_{\nu} = 1.16$  for 1320 degrees of freedom (Ta-

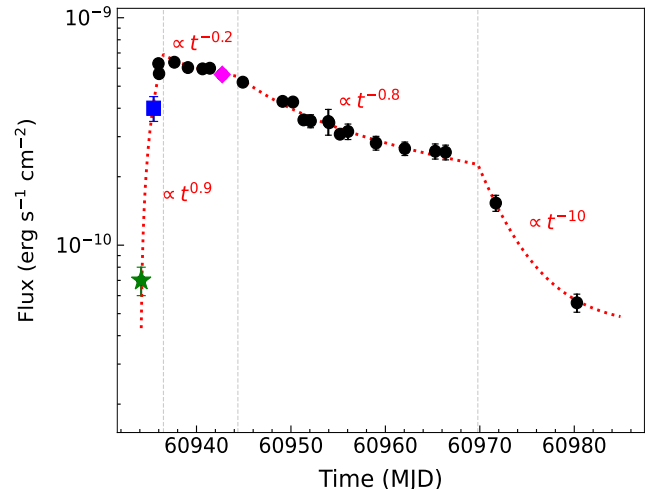


**Figure 5.** Flux evolution of EP250916a during the outburst in the 0.5–10 keV range. EP/WXT (green star), SVOM/MXT (blue square), XMM-Newton (magenta diamond), and Swift/XRT (black circles) measurements are shown. The dotted red line shows the best-fit quadruple-broken power-law model; grey vertical lines mark the break times, with the model indices indicated.

ble 2). The unabsorbed flux in the 3–80 keV range is  $(7.01 \pm 0.01) \times 10^{-10} \text{ erg cm}^{-2} \text{ s}^{-1}$ .

To characterize the broadband X-ray emission, we jointly fitted simultaneous XMM-Newton/EPIC-pn and *NuSTAR* data in the 0.5–79 keV energy range obtained on 2025 September 24. These datasets provide a comprehensive view of the broadband spectral properties during the bright, hard-state phase of the outburst. We tested multiple spectral models, including absorbed power-law, absorbed power-law plus blackbody, absorbed power-law with disk blackbody, multi-component thermal models, and Comptonization models (*comptt*). None provided satisfactory fits across the 0.5–79 keV band, primarily due to spectral residuals below  $\sim 2$  keV and a strong emission line around 0.72 keV.

A good description of the broadband continuum is obtained with an absorbed power-law modified by a partial-covering absorber, plus a Gaussian to account for the emission feature at  $0.71 \pm 0.01$  keV (equivalent width  $34 \pm 3$  eV). Adding the 0.71 keV line improves the fit by  $\Delta\chi^2 = 784$  for three additional degrees of freedom. Tentatively, this line may arise from a blend of highly ionized oxygen and Fe L-shell transitions (see, e.g. P. A. M. van Hoof 2018; G. K. Jaisawal et al. 2025b). In XSPEC notation, the final model is `constant × tbabs × tbpcf × (powerlaw + gaussian)` (Model I). The interstellar absorption is  $N_{\text{H}} = (3.3 \pm 0.5) \times 10^{21} \text{ cm}^{-2}$ , consistent with the Galactic line-of-sight value. The partial-covering absorber requires an additional column

**Table 2.** Best-fitted spectral parameters of EP250916a. The NuSTAR spectrum can be described by an absorbed power-law model. For the joint broadband NuSTAR +XMM-Newton study, Model I, Model II, and Model III are considered. Errors are quoted at the 90% confidence level.

Parameter	NuSTAR	NuSTAR + XMM-Newton		
	Power-law model	Model I	Model II	Model III
$N_{\text{H1}}$ ( $10^{22}$ cm $^{-2}$ )	$0.3 \pm 0.2$	$0.33 \pm 0.05$	$0.30 \pm 0.01$	$0.32 \pm 0.05$
$N_{\text{H2}}$ ( $10^{22}$ cm $^{-2}$ )	–	$3.9 \pm 0.2$	–	$3.8 \pm 0.3$
Covering Fraction	–	$0.27 \pm 0.01$	–	$0.24 \pm 0.01$
$kT_{\text{disk}}$ (keV)	–	–	$2.00 \pm 0.05$	–
$\text{Norm}_{\text{disk}}$	–	–	$0.24 \pm 0.03$	–
$\Gamma$	$2.03 \pm 0.01$	$2.03 \pm 0.01$	$1.89 \pm 0.01$	$1.99 \pm 0.02$
$\Gamma_{\text{Norm}}$	$0.145 \pm 0.003$	$0.148 \pm 0.002$	$0.094 \pm 0.001$	$0.140 \pm 0.004$
$E_{\text{cut}}$ (keV)	–	–	–	$262_{-64}^{+120}$
Energy (keV)	–	$0.71 \pm 0.01$	$0.72 \pm 0.01$	$0.71 \pm 0.01$
Width (keV)	–	$0.06 \pm 0.01$	$0.07 \pm 0.01$	$0.06 \pm 0.01$
Norm	–	$0.010 \pm 0.002$	$0.008 \pm 0.001$	$0.009 \pm 0.002$
Flux* ( $10^{-10}$ )	$8.45 \pm 0.04$	$8.61 \pm 0.05$	$8.49 \pm 0.06$	$8.40 \pm 0.08$
$\chi^2_{\nu}$ (dof)	1.16 (1320)	1.12 (2807)	1.13 (2807)	1.11 (2806)

\*: The 0.5–80 keV unabsorbed flux in the unit of erg cm $^{-2}$  s $^{-1}$ .

Note: Model I – absorbed power-law with a partial-covering component and Gaussian line emission; Model II – absorbed power-law with a disk blackbody component and Gaussian line emission; Model III – absorbed cutoff power-law with a partial-covering component and Gaussian line emission.

density of  $N_{\text{H2}} = (3.9 \pm 0.2) \times 10^{22}$  cm $^{-2}$  and a covering fraction of  $0.27 \pm 0.01$ , indicating clumpy or inhomogeneous material local to the source. The best fit yields  $\chi^2_{\nu} \simeq 1.12$  for 2807 degrees of freedom, with a photon index of  $\Gamma = 2.03 \pm 0.01$  and an unabsorbed 0.5–80 keV flux of  $(8.61 \pm 0.05) \times 10^{-10}$  erg cm $^{-2}$  s $^{-1}$  (see Table 2). The broadband spectrum fitted with Model I is shown in Figure 6.

As an alternative to the partial-covering component, we tested the addition of a multicolor disk blackbody (`diskbb`) to the absorbed power-law model, including the 0.7 keV Gaussian line. This model can be written as `constant × tbabs × (powerlaw + diskbb + gaussian)` (Model II). Although Model II provides a statistically comparable fit to Model I, it yields a high inner disk temperature ( $kT_{\text{disk}} \sim 2$  keV) and a low normalization ( $\text{Norm}_{\text{disk}} \sim 0.24$ ) (Table 2). Assuming a distance of 10 kpc, this normalization implies an apparent inner disk radius of  $\simeq 0.5$ – $0.8$  km for typical inclination angles ( $\theta \sim 0^\circ - 70^\circ$ ), which is smaller than expected for the innermost accretion disk radius around either a neutron star or a stellar-mass black hole. We therefore do not consider Model II as a suitable description of the continuum and adopt Model I as the preferred model for studying the 0.5–79 keV broadband emission from EP250916a with NuSTAR and XMM-Newton.

We next considered an absorbed cutoff power-law model with partial covering, `constant × tbabs ×`

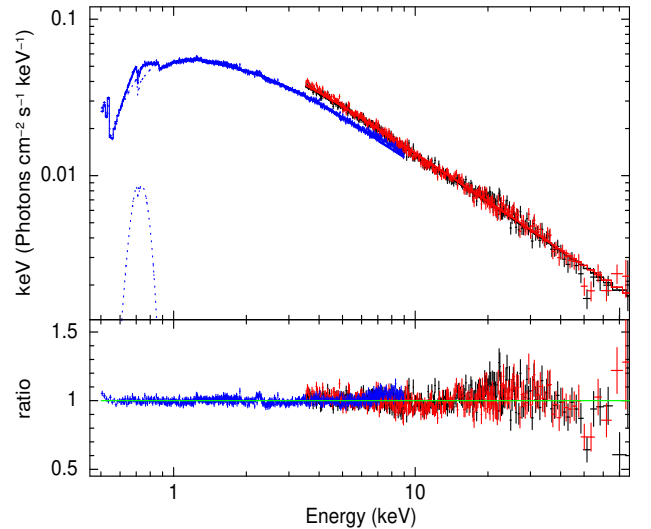


**Figure 6.** The 0.5–79 keV broadband X-ray spectra of EP250916a from XMM-Newton (blue) and NuSTAR (FPMA/FPMB; red/black) observations, fitted with an absorbed power-law model with a partial covering absorption and a Gaussian emission line (top). Spectral residuals are shown in the bottom panel.

`tbpcf × (cutoffpl + gaussian)` (Model III). This provides a statistically comparable fit ( $\chi^2_{\nu} \approx 1.11$ ), with a photon index ( $\Gamma = 1.99 \pm 0.02$ ) and a high-energy cut-off of  $E_{\text{cut}} = 262$  keV. Although the cutoff lies above the NuSTAR bandpass, the broadband data mildly prefer

a turnover consistent with weak curvature at the higher energies. The spectral parameters from Models I, II, and III are listed in Table 2 (90% confidence). No significant Fe K $\alpha$  line or Compton reflection hump is detected in either NuSTAR or XMM-Newton, suggesting an intrinsically weak reflector or a geometry in which the inner disk is truncated or weakly illuminated. The absence of any strong soft component disfavors a bright accretion disk or neutron-star boundary layer, and the lack of pulsations or thermonuclear bursts argues against a magnetized neutron star. The inferred high-energy cut-off at  $\sim 260$  keV, indicative of a very hot, optically thin Comptonizing corona often associated with black hole hard states, can support a nonthermal, Comptonization-dominated origin for the broadband emission, suggesting EP250916a as a hard X-ray transient.

## 5. DISCUSSION

We present X-ray, optical, and radio studies of the newly discovered transient EP250916a, detected in 2025 September. Our X-ray observations with Swift/XRT, NuSTAR, and XMM-Newton reveal a long-lived, spectrally hard X-ray transient, while complementary optical measurements from Swift/UVOT, Gaia, NOT/ALFOSC, and LCO provide additional constraints on the nature and physical origin of the source. Moreover, we obtained *MeerKAT* L-band (1.28 GHz) observation, which revealed no radio counterpart, placing a  $3\sigma$  upper limit of  $60 \mu\text{Jy beam}^{-1}$ .

The X-ray outburst persisted for more than 45 days between 2025 September and November, exhibiting a rapid initial rise, a plateau, and a two-stage decay. This behavior is markedly different from stellar flares, including even the most energetic superflares. For comparison, the 40 days superflare on the K2 giant HD 251108 (H. M. Günther et al. 2024; X. Mao et al. 2025) reached luminosities of  $\sim 10^{34}$  erg s $^{-1}$  and total radiated energies of  $\sim 3 \times 10^{39}$  erg, yet displayed soft ( $kT \lesssim 7$  keV) thermal plasma emission, rapid rise and decay phases, and short-lived optical brightening. EP250916a, on the other hand, shows a persistently hard X-ray spectrum, no strong high-temperature thermal component, and no rapid optical/UV brightening. Even RS CVn-like superflares cannot account for sustained spectral hardness, multi-week decay, and faint optical/UV emission, effectively ruling out stellar coronal activity as the origin.

### 5.1. Spectral Properties of EP250916a

To investigate the nature of this transient, we next examine the X-ray spectral characteristics indicative of accretion onto a compact object. Swift/XRT and NuSTAR spectra of EP250916a consistently show a hard,

nonthermal power-law ( $\Gamma \approx 1.6\text{--}2.2$ ) with no significant thermal disk component, suggesting a truncated accretion disk and a persistent hard state throughout the outburst. The hardness–intensity diagram indicates that the source remains in the hard state throughout the outburst, with XRT fluxes varying by an order of magnitude from  $(0.6\text{--}6.4) \times 10^{-10}$  erg cm $^{-2}$  s $^{-1}$ , consistent with “failed” outbursts (e.g., B. E. Tetarenko et al. 2016; A. Jana et al. 2021) where the accretion rate does not reach the soft-state threshold.

At a fiducial distance of 8 kpc, approximately the Galactic Center distance, the peak XRT flux,  $6.4 \times 10^{-10}$  erg cm $^{-2}$  s $^{-1}$  at MJD 60937.7, yields

$$L_{X,\text{peak}} \approx 4.9 \times 10^{36} \left( \frac{d}{8 \text{ kpc}} \right)^2 \text{ erg s}^{-1} \quad (1)$$

in the 0.5–10 keV band. Similarly, the broadband unabsorbed flux measured during the XMM-Newton and NuSTAR observation (MJD 60942.4–60942.9),  $8.6 \times 10^{-10}$  erg cm $^{-2}$  s $^{-1}$ , corresponds to

$$L_{\text{bol}} \approx 6.6 \times 10^{36} \left( \frac{d}{8 \text{ kpc}} \right)^2 \text{ erg s}^{-1} \quad (2)$$

over the 0.5–80 keV energy range. These luminosities place EP250916a within the faint end of the known Galactic X-ray binary population and well below the typical peak luminosities ( $\gtrsim 10^{37}$  erg s $^{-1}$ ) of classical bright black hole transients.

Broadband X-ray spectral modeling reveals a partial-covering absorber, indicative of clumpy or inhomogeneous material likely associated with the accretion flow. Partial-covering absorption has been observed in black-hole X-ray binaries, and can be attributed to clumpy inner accretion flows or disk winds (e.g., S. E. Motta et al. 2017; A. W. Shaw et al. 2022). At the same time, such absorption structures can appear in wind-fed high-mass X-ray binaries (HMXBs; G. K. Jaisawal & S. Naik 2015; G. K. Jaisawal et al. 2020), but the absence of rapid, high-amplitude X-ray flaring disfavors a classical HMXB interpretation. The observed luminosity and the slow, two-stage decay favor a low-mass X-ray binary hosting either a black hole or a weakly magnetized neutron star. Moreover, the high-energy cutoff above 30 keV is not typical for accreting NSs (see, e.g., N. E. White et al. 1983; G. K. Jaisawal et al. 2019; T. Di Salvo et al. 2023) and is more commonly associated with Comptonization in hot, radiatively inefficient flows around black holes (T. M. Belloni 2010; H. Zhu & W. Wang 2025).

In general, X-ray outburst profiles of low-mass X-ray binaries are known to exhibit a variety of morphologies, including fast-rise exponential-decay evolution, broken power-law decays, and multi-peaked decay structures

(e.g., W. Chen et al. 1997; T. A. Saraswati et al. 2025). The outburst lightcurve of EP250916a (Figure 5) is described by a quadruple broken power function, showing two step flux decay. This evolution can be understood within a disk-instability framework (e.g., A. R. King & H. Ritter 1998; G. Dubus et al. 2001). In this picture, the initial rise of the X-ray outburst is associated with the propagation of a heating front through the accretion disk, while the subsequent decay reflects cooling and depletion of the accreting material. The observed change in decay slope (Figure 5) may indicate a transition between different stages of the outburst evolution, for example from an irradiation- to a cooling-dominated phase. The two-stage flux evolution of EP250916a therefore, broadly supports this scenario, similar to that seen in the candidate black hole binary EP J182730.0–095633 (H. Q. Cheng et al. 2025).

### 5.2. QPO Feature

Timing analysis reveals no significant coherent pulsations, and the NuSTAR power spectrum is consistent with noise across  $10^{-3}$ –500 Hz, effectively excluding strongly magnetized neutron stars. A further diagnostic comes from our XMM-Newton timing analysis, which reveals a weak QPO with a characteristic frequency of  $\sim 13$  Hz. Low-frequency QPOs in black hole X-ray binaries are commonly classified as Type A, B, or C, distinguished by their coherence, amplitude, associated broadband variability, and the accretion states in which they appear (T. Belloni et al. 2002; T. M. Belloni 2010; A. R. Ingram & S. E. Motta 2019; A. Jana et al. 2022). The feature detected in EP250916a most closely resembles a Type-C-like oscillation, which is typically observed in the 0.1–30 Hz range. Its centroid frequency lies within the expected range for Type-C QPOs in intermediate states, and it is accompanied by strong, flat-topped broadband noise. This broadband variability is commonly interpreted as arising from propagating fluctuations in the mass accretion rate (T. Belloni et al. 2002). Although the coherence is modest ( $Q \sim 1.6$ ) for a Type-C QPO, the observed centroid frequency and the presence of underlying flat-topped noise exceed that expected for Type-A QPOs and are inconsistent with the narrow  $\sim 4$ –6 Hz range typical of Type-B QPOs. These properties suggest that EP250916a was in, or entering, a hard-intermediate state during the XMM-Newton observation on 2025 September 24 (MJD 60942; see the HID in Figure 2). In this context, the QPO may trace Lense–Thirring precession or other dynamical processes associated with a geometrically thick, precessing inner accretion flow (A. R. Ingram & S. E. Motta 2019).

### 5.3. Optical Counterpart: Evidence for a Low-Mass X-ray Binary?

Gaia DR3 astrometry offers additional context for the optical environment of EP250916a. Within the 2 arcsec Swift/XRT error radius, two Gaia sources are detected. Source 1, located 0.92 arcsec from the X-ray centroid, has a parallax corresponding to a geometrical distance of  $\sim 1.26$  kpc and a magnitude of  $G = 18.6$ . Adopting the observed column density  $N_{\text{H}} = (3.3 \pm 0.5) \times 10^{21} \text{ cm}^{-2}$  from our broadband spectral analysis (Table 2), and using the relation between optical extinction and hydrogen column density from T. Güver & F. Özel (2009), we obtain  $A_V \simeq 1.5 \pm 0.2$  mag. Applying the empirical relation from S. Wang & X. Chen (2019),  $A_G = 0.789 A_V$ , the corresponding extinction in the Gaia G band is  $A_G \simeq 1.2 \pm 0.2$  mag. The resulting extinction-corrected absolute magnitude of Source 1,  $M_G \simeq 6.5$ –7.2, is consistent with a mid-late K or early-mid M dwarf main-sequence star (see, e.g., B. W. Carroll & D. A. Ostlie 2006), possibly with a modest accretion-disk contribution.

Source 2, located 1.88 arcsec from the X-ray position, has  $G = 17.72$  mag, broadly consistent with our NOT/ALFOSC R-band measurement, Swift/UVOT, and LCO detection. Its astrometric solution is somewhat noisy ( $\text{RUWE} \approx 2.7$ ), possibly due to unresolved binarity or mild photocenter variability (K. El-Badry 2025). Assuming the same extinction ( $A_G \simeq 1.2 \pm 0.2$  mag), the extinction-corrected absolute magnitude for Source 2 would be  $M_G \simeq 6.0$  at 1.26 kpc,  $M_G \simeq 3.0$  at 5 kpc, and  $M_G \simeq 2.0$  at 8 kpc. An intrinsically bright counterpart with  $M_G \sim 2$  would imply an intermediate-mass donor of  $\sim 2$ –3  $M_{\odot}$  (A–F spectral type), whereas at smaller distances the photometry would instead be compatible with a late-type K–M donor (see, e.g., B. W. Carroll & D. A. Ostlie 2006). Either Gaia source could be a potential counterpart, consistent with a low-mass X-ray binary scenario.

Furthermore, LMXBs are known to show optical brightening by a few magnitudes during X-ray outbursts due to emission from the accretion disk (D. M. Russell et al. 2006; J. M. Corral-Santana et al. 2016). Both candidate counterparts have magnitudes broadly consistent with Gaia measurements obtained before the X-ray outburst, without clear evidence of strong optical brightening. This weakens the case for either source being the true counterpart. Alternatively, the system may be more distant, extremely faint, and/or heavily reddened than inferred from the X-ray column density. Future high-resolution X-ray imaging (e.g., *Chandra*) together with deeper optical/infrared observations are required to confirm the true counterpart.

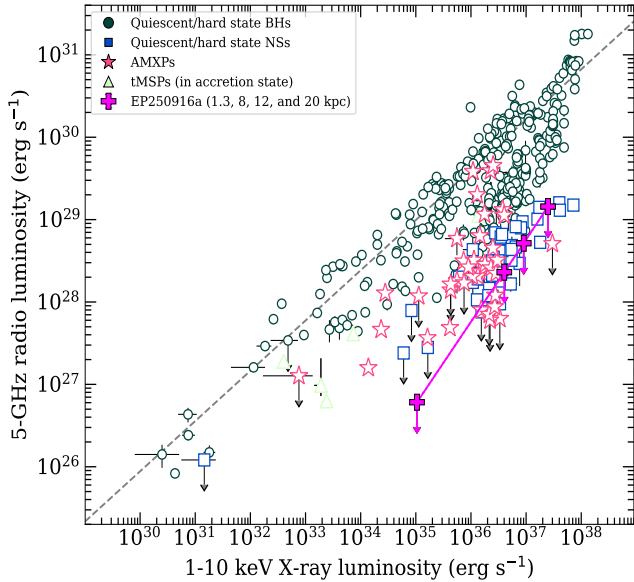


**Figure 7.** The 1–10 keV X-ray versus 5 GHz radio luminosity ( $L_R-L_X$ ) plane for accreting systems (see, e.g., A. Bahramian & A. Rushton 2022). Gray circles represent hard-state black hole LMXBs, blue squares denote hard-state neutron star LMXBs, pink stars indicate accreting millisecond X-ray pulsars (AMXPs), and light green upward triangles correspond to transitional millisecond pulsars (tMSPs). EP250916a is shown with magenta pluses, indicating  $3\sigma$  radio upper limits at  $T_0+11.4$  days, assuming distances of 1.3, 8, 12, and 20 kpc.

#### 5.4. X-ray and Radio Constraints

To place EP250916a on the  $L_R-L_X$  plane (see, e.g. S. Migliari & R. P. Fender 2006; S. Corbel et al. 2013), we estimated the 5 GHz radio luminosity using

$$L_{R,5} = 4\pi d^2 \nu S_\nu \approx 3.9 \times 10^{26} \left( \frac{S_\nu}{1 \mu\text{Jy}} \right) \left( \frac{d}{8 \text{ kpc}} \right)^2 \text{ erg s}^{-1}, \quad (3)$$

adopting a flat spectrum ( $\alpha = 0$ ) to extrapolate our *MeerKAT* 1.28 GHz  $3\sigma$  upper limit of  $60 \mu\text{Jy beam}^{-1}$  to 5 GHz. This results in  $L_{R,5} < 2.3 \times 10^{28} \text{ erg s}^{-1}$  at 8 kpc. Corresponding upper limits are  $6.1 \times 10^{26} \text{ erg s}^{-1}$  at 1.3 kpc,  $5.2 \times 10^{28} \text{ erg s}^{-1}$  at 12 kpc, and  $1.45 \times 10^{29} \text{ erg s}^{-1}$  at 20 kpc.

Figure 7 presents the  $L_R-L_X$  diagram for EP250916a. Determining the nature of the compact object in EP250916a is challenging, as there are no definitive observational signatures such as coherent pulsations, thermonuclear bursts, or dynamical mass measurements. On the 1–10 keV X-ray versus 5 GHz radio luminosity plane, its upper-limit points lie mostly within the region populated by hard-state neutron star systems, with no clear overlap with firmly established hard-state black hole systems. Nevertheless, the source shows a consistently non-

thermal X-ray spectrum with a photon index of approximately 2, a behavior often associated with black hole accretors, leaving its classification uncertain when considered solely based on the  $L_R-L_X$  plane.

#### 5.5. Nature of EP250916a and Comparison with Faint Hard-state Transients

EP250916a can be compared with a recently discovered transient EP J182730.0–095633 (EP J182730; H. Q. Cheng et al. 2025). Both sources exhibit persistently hard X-ray spectra with  $\Gamma \approx 2$ . However, their temporal evolution differs significantly. EP J182730 experienced a short, steep outburst lasting approximately three weeks, with its X-ray luminosity declining by about three orders of magnitude. In contrast, EP250916a displays a more gradual decay, including a plateau phase, indicating a slower change in accretion rate. EP J182730 also exhibited stronger absorption, a prominent 40 mHz QPO, and an inverted radio spectrum indicative of a compact jet, although the source was not detected in the L-band early in the outburst, similar to EP250916a. Its infrared counterpart is heavily reddened. By comparison, EP250916a shows milder absorption, only faint optical counterparts within the X-ray error region, a weaker Type-C-like low-frequency QPO around 13 Hz, and no detected radio emission during the *MeerKAT* L-band observation. These contrasts illustrate the diversity among faint, hard-state X-ray transients, ranging from heavily obscured, jet-dominated systems to lower-accretion-rate objects such as EP250916a.

Historically, most black hole X-ray binaries have been discovered during bright outbursts ( $\gtrsim 10^{37} \text{ erg s}^{-1}$ ), reflecting the sensitivity of all-sky monitors to high-luminosity events that undergo canonical state transitions. A small subset of sources such as Swift J1357.2–0933 (J. M. Corral-Santana et al. 2013), XTE J1118+480 (R. M. Wagner et al. 2001), XTE J1728–295 (R. Walter et al. 2004), CXOGC J174540.0–290031 (D. Porquet et al. 2005), and EP J182730 (H. Q. Cheng et al. 2025) have been identified during intrinsically faint outbursts ( $L_X \lesssim 10^{36} \text{ erg s}^{-1}$ ), in addition to increasing number of very faint X-ray transients (VFXTs; see, e.g., A. R. King & R. Wijnands 2006). EP250916a adds to this sparsely sampled population, illustrating the increasing ability of modern high-cadence X-ray facilities to uncover low-luminosity, hard-state accretors.

The long-duration outburst, persistently hard spectrum, faint optical counterpart, moderate luminosity, and tentative Type-C-like QPO support the interpretation of EP250916a as an accreting compact object, most likely a black hole candidate rather than a stellar

flare or from an extragalactic source. Its behaviour reinforces the emerging picture of a diverse population of faint, hard-state X-ray transients revealed by contemporary time-domain surveys.

## 6. CONCLUSIONS

We have presented a comprehensive multiwavelength study of the hard X-ray transient EP250916a, discovered by the Einstein Probe on 2025 September 16. Follow-up observations with Swift/XRT, NuSTAR, XMM-Newton, the NOT, LCO, and *MeerKAT* provide a detailed view of its temporal, spectral, optical, and radio behavior. EP250916a exhibits a rapid initial X-ray brightening followed by a broad plateau and a two-stage decay lasting over 40 days, consistent with a sustained accretion event rather than a short-lived stellar flare. Its X-ray spectrum is persistently hard ( $\Gamma \approx 1.6\text{--}2.2$ ), dominated by nonthermal emission. Broadband spectral modeling favors a power-law or cutoff power-law continuum modified by partial-covering absorption, indicative of clumpy or inhomogeneous material in the local environment.

Our timing analysis with NuSTAR reveals no coherent pulsations or thermonuclear bursts, but XMM-Newton detects a weak  $\sim 13$  Hz QPO with properties most consistent with a Type-C-like oscillation. The presence of strong broadband noise and a moderately coherent peak suggests that EP250916a was in, or entering, a hard-intermediate state during the XMM-Newton observation. This QPO detection can provide evidence for dynamical processes in a geometrically thick inner accretion flow, possibly linked to Lense–Thirring precession, and strengthens the case that EP250916a is an accreting compact object rather than a stellar flare or from an extragalactic source.

The X-ray luminosity places EP250916a at the faint end of the Galactic X-ray binary population. Most transient black hole X-ray binaries have been discovered during bright outbursts ( $L_X \gtrsim 10^{37}$  erg s $^{-1}$ ), making systems like EP250916a relatively rare and highlighting the importance of sensitive, wide-field monitoring for identifying low-luminosity events. Comparisons with similar faint, hard X-ray transients, such as

EP J182730.0–095633, suggest that EP250916a may belong to an emerging population of low-luminosity, hard-state X-ray binaries or VFXTs. Variations in absorption, timing properties, and optical/infrared characteristics across these sources emphasize the diversity of accretion environments and system configurations within this class. Thus, EP250916a represents a long-duration, hard-state X-ray transient powered by accretion onto a compact object, likely a stellar-mass black hole.

## ACKNOWLEDGMENTS

We sincerely thank the referee for constructive suggestions on the paper. This work was supported by NASA through the Astrophysics Explorers Program and made use of data and software provided by the High Energy Astrophysics Science Archive Research Center (HEASARC). The data presented here were obtained with ALFOSC, which is provided by the Instituto de Astrofísica de Andalucía (IAA) under a joint agreement with the University of Copenhagen and NOT. The MeerKAT telescope is operated by the South African Radio Astronomy Observatory, which is a facility of the National Research Foundation, an agency of the Department of Science and Innovation. This work was carried out in part using facilities and data processing pipelines developed at the Inter-University Institute for Data Intensive Astronomy (IDIA). IDIA is a partnership of the Universities of Cape Town, the Western Cape, and Pretoria. This work received financial support from INAF through the GRAWITA 2022 Large Program Grant. DMR and DA are supported by Tamkeen under the NYU Abu Dhabi Research Institute grant CASS. GL was supported by a research grant (VIL60862) from VILLUM FONDEN.

*Facilities:* Swift(XRT and UVOT), NuSTAR, XMM-Newton, Gaia, NOT:2.56m, LCO:1m, MeerKAT

*Software:* astropy (Astropy Collaboration et al. 2013, 2018, 2022), HEASoft (Nasa High Energy Astrophysics Science Archive Research Center (Heasarc) 2014), XSPEC (K. A. Arnaud 1996), CASA (CASA Team et al. 2022)

## REFERENCES

Arnaud, K. A. 1996, in *Astronomical Society of the Pacific Conference Series*, Vol. 101, *Astronomical Data Analysis Software and Systems V*, ed. G. H. Jacoby & J. Barnes,

Astropy Collaboration, Robitaille, T. P., Tollerud, E. J., et al. 2013, *A&A*, 558, A33, doi: [10.1051/0004-6361/201322068](https://doi.org/10.1051/0004-6361/201322068)

Astropy Collaboration, Price-Whelan, A. M., Sipőcz, B. M., et al. 2018, *AJ*, 156, 123, doi: [10.3847/1538-3881/aabc4f](https://doi.org/10.3847/1538-3881/aabc4f)

- Astropy Collaboration, Price-Whelan, A. M., Lim, P. L., et al. 2022, *ApJ*, 935, 167, doi: [10.3847/1538-4357/ac7c74](https://doi.org/10.3847/1538-4357/ac7c74)
- Atteia, J.-L., Cordier, B., & Wei, J. 2022, *International Journal of Modern Physics D*, 31, 2230008, doi: [10.1142/S0218271822300087](https://doi.org/10.1142/S0218271822300087)
- Atwood, W. B., Abdo, A. A., Ackermann, M., et al. 2009, *ApJ*, 697, 1071, doi: [10.1088/0004-637X/697/2/1071](https://doi.org/10.1088/0004-637X/697/2/1071)
- Bahramian, A., & Degenaar, N. 2023, in *Handbook of X-ray and Gamma-ray Astrophysics*, 120, doi: [10.1007/978-981-16-4544-0\\_94-1](https://doi.org/10.1007/978-981-16-4544-0_94-1)
- Bahramian, A., & Rushton, A. 2022, *bersavosh/XRB-LrLx\_pub: update 20220908, v220908 Zenodo*, doi: [10.5281/zenodo.7059313](https://doi.org/10.5281/zenodo.7059313)
- Belloni, T., Psaltis, D., & van der Klis, M. 2002, *ApJ*, 572, 392, doi: [10.1086/340290](https://doi.org/10.1086/340290)
- Belloni, T. M. 2010, in *Lecture Notes in Physics*, Berlin Springer Verlag, ed. T. Belloni, Vol. 794, 53, doi: [10.1007/978-3-540-76937-8\\_3](https://doi.org/10.1007/978-3-540-76937-8_3)
- Camilo, F., Scholz, P., Serylak, M., et al. 2018, *ApJ*, 856, 180, doi: [10.3847/1538-4357/aab35a](https://doi.org/10.3847/1538-4357/aab35a)
- Carroll, B. W., & Ostlie, D. A. 2006, *An introduction to modern astrophysics and cosmology*
- CASA Team, Bean, B., Bhatnagar, S., et al. 2022, *PASP*, 134, 114501, doi: [10.1088/1538-3873/ac9642](https://doi.org/10.1088/1538-3873/ac9642)
- Cash, W. 1979, *ApJ*, 228, 939, doi: [10.1086/156922](https://doi.org/10.1086/156922)
- Chen, W., Shrader, C. R., & Livio, M. 1997, *ApJ*, 491, 312, doi: [10.1086/304921](https://doi.org/10.1086/304921)
- Cheng, H. Q., Zhao, Q. C., Tao, L., et al. 2025, *ApJL*, 991, L41, doi: [10.3847/2041-8213/adf104](https://doi.org/10.3847/2041-8213/adf104)
- Coleiro, A., Maggi, P., Cangemi, F., & Lachaud, C. 2025, *The Astronomer's Telegram*, 17396, 1
- Corbel, S., Coriat, M., Brocksopp, C., et al. 2013, *MNRAS*, 428, 2500, doi: [10.1093/mnras/sts215](https://doi.org/10.1093/mnras/sts215)
- Corral-Santana, J. M., Casares, J., Muñoz-Darias, T., et al. 2016, *A&A*, 587, A61, doi: [10.1051/0004-6361/201527130](https://doi.org/10.1051/0004-6361/201527130)
- Corral-Santana, J. M., Casares, J., Muñoz-Darias, T., et al. 2013, *Science*, 339, 1048, doi: [10.1126/science.1228222](https://doi.org/10.1126/science.1228222)
- Dai, C. Y., Wu, Q. Y., Li, D. Y., & Pan, H. W. 2025a, *The Astronomer's Telegram*, 17395, 1
- Dai, C. Y., Wu, Q. Y., Li, D. Y., Pan, H. W., & Einstein Probe Team. 2025b, *GRB Coordinates Network*, 41861, 1
- D'Avanzo, P. 2015, *Journal of High Energy Astrophysics*, 7, 73, doi: [10.1016/j.jheap.2015.07.002](https://doi.org/10.1016/j.jheap.2015.07.002)
- Di Salvo, T., Papitto, A., Marino, A., Iaria, R., & Burderi, L. 2023, in *Handbook of X-ray and Gamma-ray Astrophysics*, 147, doi: [10.1007/978-981-16-4544-0\\_103-1](https://doi.org/10.1007/978-981-16-4544-0_103-1)
- Done, C., Gierliński, M., & Kubota, A. 2007, *A&A Rv*, 15, 1, doi: [10.1007/s00159-007-0006-1](https://doi.org/10.1007/s00159-007-0006-1)
- Dubus, G., Hameury, J.-M., & Lasota, J.-P. 2001, *A&A*, 373, 251, doi: [10.1051/0004-6361:20010632](https://doi.org/10.1051/0004-6361:20010632)
- El-Badry, K. 2025, *The Open Journal of Astrophysics*, 8, 62, doi: [10.33232/001c.138448](https://doi.org/10.33232/001c.138448)
- Evans, P. A., Beardmore, A. P., Page, K. L., et al. 2009, *MNRAS*, 397, 1177, doi: [10.1111/j.1365-2966.2009.14913.x](https://doi.org/10.1111/j.1365-2966.2009.14913.x)
- Gaia Collaboration, Vallenari, A., Brown, A. G. A., et al. 2023, *A&A*, 674, A1, doi: [10.1051/0004-6361/202243940](https://doi.org/10.1051/0004-6361/202243940)
- Gehrels, N., Chincarini, G., Giommi, P., et al. 2004, *ApJ*, 611, 1005, doi: [10.1086/422091](https://doi.org/10.1086/422091)
- Goad, M. R., Tyler, L. G., Beardmore, A. P., et al. 2007, *A&A*, 476, 1401, doi: [10.1051/0004-6361:20078436](https://doi.org/10.1051/0004-6361:20078436)
- Günther, H. M., Pasham, D., Binks, A., et al. 2024, *ApJ*, 977, 6, doi: [10.3847/1538-4357/ad8b2c](https://doi.org/10.3847/1538-4357/ad8b2c)
- Güver, T., & Özel, F. 2009, *MNRAS*, 400, 2050, doi: [10.1111/j.1365-2966.2009.15598.x](https://doi.org/10.1111/j.1365-2966.2009.15598.x)
- Harrison, F. A., Craig, W. W., Christensen, F. E., et al. 2013, *ApJ*, 770, 103, doi: [10.1088/0004-637X/770/2/103](https://doi.org/10.1088/0004-637X/770/2/103)
- Heywood, I. 2020, *oxkat: Semi-automated imaging of MeerKAT observations*, *Astrophysics Source Code Library*, record ascl:2009.003
- HI4PI Collaboration, Ben Bekhti, N., Flöer, L., et al. 2016, *A&A*, 594, A116, doi: [10.1051/0004-6361/201629178](https://doi.org/10.1051/0004-6361/201629178)
- Homan, J., & Belloni, T. 2005, *Ap&SS*, 300, 107, doi: [10.1007/s10509-005-1197-4](https://doi.org/10.1007/s10509-005-1197-4)
- Hugo, B. V., Perkins, S., Merry, B., Mauch, T., & Smirnov, O. M. 2022, in *Astronomical Society of the Pacific Conference Series*, Vol. 532, *Astronomical Society of the Pacific Conference Series*, ed. J. E. Ruiz, F. Pierfederici, & P. Teuben, 541, doi: [10.48550/arXiv.2206.09179](https://doi.org/10.48550/arXiv.2206.09179)
- Illiano, G., Zanon, A. M., Sbarufatti, B., et al. 2025, *The Astronomer's Telegram*, 17397, 1
- Ingram, A. R., & Motta, S. E. 2019, *NewAR*, 85, 101524, doi: [10.1016/j.newar.2020.101524](https://doi.org/10.1016/j.newar.2020.101524)
- Jaisawal, G. K., Chenevez, J., Illiano, G., Sanna, A., & Zhao, Q. C. 2025a, *The Astronomer's Telegram*, 17421, 1
- Jaisawal, G. K., & Naik, S. 2015, *MNRAS*, 448, 620, doi: [10.1093/mnras/stv029](https://doi.org/10.1093/mnras/stv029)
- Jaisawal, G. K., Naik, S., Ho, W. C. G., et al. 2020, *MNRAS*, 498, 4830, doi: [10.1093/mnras/staa2604](https://doi.org/10.1093/mnras/staa2604)
- Jaisawal, G. K., Wilson-Hodge, C. A., Fabian, A. C., et al. 2019, *ApJ*, 885, 18, doi: [10.3847/1538-4357/ab4595](https://doi.org/10.3847/1538-4357/ab4595)
- Jaisawal, G. K., Chenevez, J., Strohmayer, T. E., et al. 2025b, *ApJ*, 986, 16, doi: [10.3847/1538-4357/adcc24](https://doi.org/10.3847/1538-4357/adcc24)
- Jana, A., Naik, S., Jaisawal, G. K., et al. 2022, *MNRAS*, 511, 3922, doi: [10.1093/mnras/stac315](https://doi.org/10.1093/mnras/stac315)
- Jana, A., Jaisawal, G. K., Naik, S., et al. 2021, *Research in Astronomy and Astrophysics*, 21, 125, doi: [10.1088/1674-4527/21/5/125](https://doi.org/10.1088/1674-4527/21/5/125)
- Jansen, F., Lumb, D., Altieri, B., et al. 2001, *A&A*, 365, L1, doi: [10.1051/0004-6361:20000036](https://doi.org/10.1051/0004-6361:20000036)

- Jonas, J., & MeerKAT Team. 2016, in MeerKAT Science: On the Pathway to the SKA, 1, doi: [10.22323/1.277.0001](https://doi.org/10.22323/1.277.0001)
- King, A. R., & Ritter, H. 1998, MNRAS, 293, L42, doi: [10.1046/j.1365-8711.1998.01295.x](https://doi.org/10.1046/j.1365-8711.1998.01295.x)
- King, A. R., & Wijnands, R. 2006, MNRAS, 366, L31, doi: [10.1111/j.1745-3933.2005.00126.x](https://doi.org/10.1111/j.1745-3933.2005.00126.x)
- Komossa, S. 2015, Journal of High Energy Astrophysics, 7, 148, doi: [10.1016/j.jheap.2015.04.006](https://doi.org/10.1016/j.jheap.2015.04.006)
- Kouveliotou, C., Wijers, R. A. M. J., & Woosley, S. 2012, Gamma-ray Bursts
- Lang, D., Hogg, D. W., Mierle, K., Blanton, M., & Roweis, S. 2010, AJ, 139, 1782, doi: [10.1088/0004-6256/139/5/1782](https://doi.org/10.1088/0004-6256/139/5/1782)
- Lewin, W. H. G., van Paradijs, J., & van den Heuvel, E. P. J. 1997, X-ray Binaries
- Maehara, H., Shibayama, T., Notsu, S., et al. 2012, Nature, 485, 478, doi: [10.1038/nature11063](https://doi.org/10.1038/nature11063)
- Mao, X., Liu, H.-Y., Wang, S., et al. 2025, ApJ, 980, 268, doi: [10.3847/1538-4357/ada698](https://doi.org/10.3847/1538-4357/ada698)
- Matsuoka, M., Kawasaki, K., Ueno, S., et al. 2009, PASJ, 61, 999, doi: [10.1093/pasj/61.5.999](https://doi.org/10.1093/pasj/61.5.999)
- Merloni, A., Predehl, P., Becker, W., et al. 2012, arXiv e-prints, arXiv:1209.3114, doi: [10.48550/arXiv.1209.3114](https://doi.org/10.48550/arXiv.1209.3114)
- Migliari, S., & Fender, R. P. 2006, MNRAS, 366, 79, doi: [10.1111/j.1365-2966.2005.09777.x](https://doi.org/10.1111/j.1365-2966.2005.09777.x)
- Motta, S. E., Kajava, J. J. E., Sánchez-Fernández, C., Giustini, M., & Kuulkers, E. 2017, MNRAS, 468, 981, doi: [10.1093/mnras/stx466](https://doi.org/10.1093/mnras/stx466)
- Nasa High Energy Astrophysics Science Archive Research Center (Heasarc). 2014, HEASoft: Unified Release of FTOOLS and XANADU., Astrophysics Source Code Library, record ascl:1408.004 <http://ascl.net/1408.004>
- Offringa, A. R., McKinley, B., Hurley-Walker, N., et al. 2014, MNRAS, 444, 606, doi: [10.1093/mnras/stu1368](https://doi.org/10.1093/mnras/stu1368)
- Okamoto, S., Notsu, Y., Maehara, H., et al. 2021, ApJ, 906, 72, doi: [10.3847/1538-4357/abc8f5](https://doi.org/10.3847/1538-4357/abc8f5)
- Porquet, D., Grosso, N., Burwitz, V., et al. 2005, A&A, 430, L9, doi: [10.1051/0004-6361:200400117](https://doi.org/10.1051/0004-6361:200400117)
- Revnivtsev, M., Sazonov, S., Jahoda, K., & Gilfanov, M. 2004, A&A, 418, 927, doi: [10.1051/0004-6361:20035798](https://doi.org/10.1051/0004-6361:20035798)
- Russell, D. M., Fender, R. P., Hynes, R. I., et al. 2006, MNRAS, 371, 1334, doi: [10.1111/j.1365-2966.2006.10756.x](https://doi.org/10.1111/j.1365-2966.2006.10756.x)
- Saraswati, T. A., Vierdayanti, K., & Premadi, P. W. 2025, MNRAS, 537, 1146, doi: [10.1093/mnras/staf042](https://doi.org/10.1093/mnras/staf042)
- Shaw, A. W., Miller, J. M., Grinberg, V., et al. 2022, MNRAS, 516, 124, doi: [10.1093/mnras/stac2213](https://doi.org/10.1093/mnras/stac2213)
- Strüder, L., Briel, U., Dennerl, K., et al. 2001, A&A, 365, L18, doi: [10.1051/0004-6361:20000066](https://doi.org/10.1051/0004-6361:20000066)
- Tetarenko, B. E., Sivakoff, G. R., Heinke, C. O., & Gladstone, J. C. 2016, ApJS, 222, 15, doi: [10.3847/0067-0049/222/2/15](https://doi.org/10.3847/0067-0049/222/2/15)
- van Hoof, P. A. M. 2018, Galaxies, 6, 63, doi: [10.3390/galaxies6020063](https://doi.org/10.3390/galaxies6020063)
- Verner, D. A., Ferland, G. J., Korista, K. T., & Yakovlev, D. G. 1996, ApJ, 465, 487, doi: [10.1086/177435](https://doi.org/10.1086/177435)
- Wagner, R. M., Foltz, C. B., Shahbaz, T., et al. 2001, ApJ, 556, 42, doi: [10.1086/321572](https://doi.org/10.1086/321572)
- Walter, R., Bodaghee, A., Barlow, E. J., et al. 2004, The Astronomer's Telegram, 229, 1
- Wang, S., & Chen, X. 2019, ApJ, 877, 116, doi: [10.3847/1538-4357/ab1c61](https://doi.org/10.3847/1538-4357/ab1c61)
- White, N. E., Swank, J. H., & Holt, S. S. 1983, ApJ, 270, 711, doi: [10.1086/161162](https://doi.org/10.1086/161162)
- Wilms, J., Allen, A., & McCray, R. 2000, ApJ, 542, 914, doi: [10.1086/317016](https://doi.org/10.1086/317016)
- Winkler, C., Courvoisier, T. J.-L., Di Cocco, G., et al. 2003, A&A, 411, L1, doi: [10.1051/0004-6361:20031288](https://doi.org/10.1051/0004-6361:20031288)
- Yuan, W., Zhang, C., Chen, Y., & Ling, Z. 2022, in Handbook of X-ray and Gamma-ray Astrophysics, ed. C. Bambi & A. Sanganelo, 86, doi: [10.1007/978-981-16-4544-0\\_151-1](https://doi.org/10.1007/978-981-16-4544-0_151-1)
- Zhu, H., & Wang, W. 2025, Galaxies, 13, 111, doi: [10.3390/galaxies13050111](https://doi.org/10.3390/galaxies13050111)